Interplay between intrinsic defects, doping, and free carrier concentration in SrTiO_{3} thin films

Elif Ertekin, Varadharajan Srinivasan, Jayakanth Ravichandran, Pim B. Rossen, Wolter Siemons, Arun Majumdar, Ramamoorthy Ramesh, and Jeffrey C. Grossman

Phys. Rev. B **85**, 195460 — Published 29 May 2012

DOI: 10.1103/PhysRevB.85.195460

Interplay between Intrinsic Defects, Doping, and Free Carrier Concentration in Strontium Titanate

Elif Ertekin,[1,*] Varadharajan Srinivasan,[2] Jayakanth Ravichandran,[3,4] Pim B. Rossen,[5] Wolter Siemons,[6] Arun Majumdar,[7] Ramamoorthy Ramesh,[5,4,8] and Jeffrey C. Grossman[1,†]

[1] *Dept. of Materials Science & Engineering, Massachusetts Institute of Technology, Cambridge, MA 02139*
[2] *Dept. of Chemistry, Indian Institute of Science Education and Research, Bhopal, India*
[3] *Applied Science & Technology Graduate Group, University of California, Berkeley, CA 94720*
[4] *Materials Sciences Division, Lawrence Berkeley National Laboratory, Berkeley, CA 94720*
[5] *Dept. of Materials Science & Engineering, University of California, Berkeley, CA 94720*
[6] *Materials Science and Technology Division, Oak Ridge National Laboratory, Oak Ridge, TN 37831*
[7] *ARPA–E, U.S. Department of Energy, 1000 Independence Avenue, Washington, D.C. 20585*
[8] *STEP, U.S. Department of Energy, 1000 Independence Avenue, Washington, D.C. 20585*

(Dated: May 4, 2012)

Using both computational and experimental analysis, we demonstrate a rich point–defect phase diagram in doped strontium titanate as a function of thermodynamic variables such as oxygen partial pressure and electronic chemical potential. Computational modeling of point–defect energetics demonstrates that a complex interplay exists between dopants, thermodynamic parameters, and intrinsic defects in thin films of $SrTiO_3$ (STO). We synthesize STO thin films via pulsed laser deposition and explore this interplay between intrinsic defects, doping, compensation, and carrier concentration. Our point–defect analysis (i) demonstrates that careful control over growth conditions can result in the tunable presence of anion and cation vacancies, (ii) suggests that compensation mechanisms will pose intrinsic limits to the dopability of perovskites, and (iii) provides a guide for tailoring the properties of doped perovskite thin films.

I. INTRODUCTION

The exceptional scope of properties exhibited by perovskite (ABO_3) oxides has catapulted these materials to the forefront of recent research efforts[1–4]. Thin films made from these materials exhibit multiferroicity[3,4], piezoelectricity[5], magnetism[6], colossal magnetoresistance[7], and ferroelectricity[8], as well as conductivities that range from insulating to metallic to superconducting[9]. When distinct oxides are deposited in succession on the same substrate, many of these properties can be coupled across heteroepitaxial interfaces. This concept underlies the fields of oxide–based electronics and spintronics, with applications in ultra–low power and high–performance switching, memories, and logic[4,8,10,11]. Device–quality materials, however, require precise control of doping, impose severe demands on film stoichiometry, and require stringent limits on allowable concentrations of unwanted defects. Currently, the (often uncontrolled) presence of defects influences and can even dominate the properties of oxides[10,12–14]. Particularly for low carrier density systems, very small (e.g. 10^{18} cm^{-3}) differences in defect densities have a striking impact on film properties, particularly electrical properties such as carrier density[15–17].

In this contribution, we explore the equilibrium thermodynamics of point defects in STO as a function of thermodynamic variables such as oxygen partial pressure and electron chemical potential (Fermi energy). We use density functional theory (DFT) to predict the defect phase diagram for STO and develop a comprehensive point defect analysis that accounts for the varied defects possibilities in STO. To complement the theoretical predictions, we analyze the stoichiometry of STO thin films grown by PLD and show that at extreme thermodynamic conditions, experimental observations are in line with the theoretical predictions. Typically, PLD grown films are analyzed for defects and non-stoichiometry as a function of laser fluence. In this analysis, we highlight the importance of other thermodynamic variables by fixing the laser fluence. This analysis elucidates the crucial role of growth conditions on the types and concentrations of defects that are present and their interplay. It: (i) demonstrates that the defect profile in these thin films exhibits a large sensitivity to the prevailing growth conditions, (ii) confirms recent experimental evidence that both anion and cation vacancies are present in PLD–grown perovskite–oxide films[17,18], (iii) suggests that operative compensation mechanisms pose intrinsic limits to dopability in oxides, and (iv) indicates that careful control over the growth conditions may enable tuning of film composition, defect distribution, and resulting properties such as optical emission[19], thereby enabling the realization of functional components such as transparent conducting oxides[20].

Vacancies and their complexes are the dominant point defects in most perovskites, and their presence influences electron mobility[15], electrical conductivity[16], and physical properties such as defect–induced ferroelectricity in STO[13,14] and defect–driven changes to the thermal conductivity[21]. Perovskite oxide films are often grown by pulsed laser deposition (PLD) due to its ability to retain stoichiometric cationic transfer when the material is ablated with a laser fluence above the threshold for the material. Recent careful studies on the growth of STO thin films[16,18] have suggested that in STO only a narrow laser fluence range can provide stoichiometric transfer. The defect distribution in thin films realized with high–energy techniques such as PLD are likely dominated by kinetic effects and possible stoichiometric deviations at fractions of a percent. In contrast, low–energy techniques such as molecular beam epitaxy (MBE) may yield compositions closer to stoichiometric and/or defect distributions that are more closely governed by thermodynamics[22,23]. For example, recently, controlled doping and carrier mobilities as high as 30,000 cm^2 V^{-1} s^{-1} (exceeding those of single crystals) have been demonstrated for epitaxial heterostructures of STO realized by MBE[15]. Further, the suppression of cation vacancies has been demonstrated to be consistent with the realization of high doping efficiencies and high mobilities in MBE–grown La–doped STO thin films[24]. It is worth noting that the doping control required to achieve such high mobility is close to a few parts per million (ppm).

We choose doped STO as our model perovskite oxide because it exhibits a large range of measured properties from insulating to superconducting[9], and because impurity doping of this system has been extensively characterized. STO is largely susceptible to donor doping by cation substitution and via the presence of oxygen vacancies. For example, Lanthanum (La), as a substitutional species at the Sr site, is well–understood to be an electron donor[25,26]; under carefully controlled growth conditions, a clear correspondence is established in which one conduction electron is created per La substitution[15]. In STO, the existence of oxygen vacancies (V_O) has long been documented in the literature as well; they are known electron donors[25,26] that are typically believed to exist in most heterostructures[27]. V_O are also associated with clustering[28], blue light emission[19], superconductivity[29], and have been implicated in the high conductivites at the STO/$LaAlO_3$ interface[30]. Understanding the interplay between these vacancies, doping, and other intrinsic defects is critical as high quality heterostructures with STO are currently avidly pursued for thermoelectric applications[31], defect[13,14] or strain[32] –induced ferroelectricity, electric field induced superconductivity[33], and two-dimensional interface conductivity[34]. However, to truly understand this system, a key question is whether the observed phenomena arise either intrinsically or from specious effects due to unknown and undesired defect distributions.

II. COMPUTATION

To determine the types of intrinsic defects – vacancies and their complexes – that are energetically favorable in STO, we first systematically determine defect formation energies for a variety of candidate defects. We expect this comprehensive understanding of stoichiometry and point defects will be most useful for analyzing the properties of thin films synthesized under equilibrium processes. However, although the defect distributions that are present in thin films grown by non–equilibrium techniques are likely governed by kinetic effects, knowledge of defect formation energies as predicted by thermodynamic considerations may still be qualitatively useful even for PLD–grown thin films. A number of previous calculations of defect formation energies in STO have been reported previously – for example Refs. [26, 28, 35, and 36] – here we present a comprehensive and systematic study for a variety of defects and defect complexes under a wide range of environmental conditions.

A. Density Functional Theory

We perform calculations based on density functional theory (DFT) to determine the formation energies for a variety of native defects, including isolated Sr, Ti, and O vacancies (V_{Sr}, V_{Ti}, V_O), Schottky defects (V_{SrO}), O divacancies (V_{OO})[28], and complexes of Schottky defects and O vacancies ($V_{SrOO,a}$ and $V_{SrOO,b}$, see Ref. [35]). In our calculations, we employ a plane wave DFT framework using the QUANTUM–ESPRESSO package[37], and simulate point defects in a $4 \times 4 \times 4$ supercell containing 320 atoms and k–points sampled via a $2 \times 2 \times 2$ Monkhorst–Pack scheme.

Core electrons are modeled via ultrasoft pseudopotentials[38], and semicore electrons are included for both Sr and Ti. Total energies are calculated using a generalized gradient approximation to the exchange correlation functional according to the Perdew–Burke–Ernzerhoff (PBE) scheme[39] and a plane wave kinetic energy cutoff of 30 Ry. For bulk STO, under these parameters DFT–PBE predicts a lattice constant of 3.94 Å(experimental: 3.91 Å), an indirect band gap of 1.82 eV (experimental 3.25 eV), and a good description of the cohesive energy (see Table I). For supercells containing defects, the atomic coordinates are internally relaxed until the Hellmann–Feynman force acting on each atom is less than 3 meV/Å.

To explore charged defects, electrons are either added to or removed from the supercell containing the defect in the calculation. Since the total energy of a charged supercell with periodic boundary conditions diverges, a compensating jellium background charge is automatically incorporated to render the total energy convergent. Since computed total energies are given with respect to the average electrostatic potential, a potential alignment technique (described below) is used to enable direct comparison of energies for supercells with different charge states.

B. Thermodynamic Framework

We compute the defect–formation energies $\Delta E_{D,q}$ as

$$\Delta E_{D,q} = (E_{D,q} - E_{perf}) - \sum_i n_i \mu_i + q(E_V + E_F) \ , \tag{1}$$

where $E_{D,q}$ is the (DFT–computed) total energy of the supercell containing a defect D in the charge state q, E_{perf} is the (DFT–computed) total energy of the perfect supercell, and n_i is the number of atoms of species i added to ($n_i > 0$) or removed from ($n_i < 0$) the supercell to create the defect[40]. Different growth conditions are accommodated by the set of chemical potentials $\mu_i = \mu_i^{bulk} + \Delta\mu_i$ for each element by assuming that each is in equilibrium with a physical reservoir such as a gas or a bulk phase. E_V is the energy of the valence band maximum, and E_F is the Fermi energy referenced to E_V so that $0 \leq E_F \leq E_g$ where E_g is the band gap.

At equilibrium, the atomic chemical potentials satisfy $\Delta\mu_{Sr} + \Delta\mu_{Ti} + 3\Delta\mu_O = \Delta\mu_{STO}$. As both temperature T and P_{O_2} are controlled during growth, μ_O is fixed as

$$\mu_O(T, P_{O_2}) = \frac{1}{2}\mu^o_{O_2}(T, P^o_{O_2}) + \frac{1}{2}k_B T \ln\left(\frac{P_{O_2}}{P^o_{O_2}}\right) \ , \tag{2}$$

where k_B is the Boltzmann constant and $\mu^o_{O_2}(T, P^o_{O_2} = 1 \text{ atm})$ is the free energy of molecular oxygen. We confine our analysis to the part of chemical potential phase space in which STO is stable, and the precipitation of bulk Sr and Ti is not: $\Delta\mu_{Sr} < 0$, $\Delta\mu_{Ti} < 0$ (large triangle in Fig. 1). We further restrict our analysis near to or within regions where the formation of compounds SrO, TiO, and TiO_2 is not favorable, also indicated in Fig. 1. This amounts to the constraints $\Delta\mu_O + \Delta\mu_{Sr} \leq \mu_{SrO}$, etc. The DFT–computed phase boundaries are in good agreement with those

from experiment; see Table I. In our subsequent analysis, we consider three paths λ^i, $i = 1, 2, 3$ through phase space in Fig. 1, each parametrized by $\Delta\mu_O$. λ^1 corresponds to nominally "normal" Sr/Ti stoichiometry, while λ^2 and λ^3 correspond to Sr poor and Ti poor growth, respectively. Along each individual path λ^i, $\Delta\mu_O$ is varied to consider the full range of oxygen poor ($\Delta\mu_O = \Delta\mu_O^{min}$) to oxygen rich ($\Delta\mu_O = 0$) growth.

Formation energy	DFT-PBE	experiment
SrO (rocksalt)	-5.93	-6.14 (Ref. [41])
TiO (rocksalt)	-5.05	-5.62 (Ref. [41])
TiO_2 (rutile)	-10.00	-9.73 (Ref. [41])
STO (cubic)	-1.21	-1.4 (Ref. [42])

TABLE I. Comparison of DFT–computed and experimental bulk formation energies of SrO, TiO, TiO_2, and STO (eV/formula unit). The formation energies of SrO, TiO, and TiO_2 are given with respect to bulk Sr, bulk Ti, and O_2 molecule; the formation energy of STO is given with respect to SrO and TiO_2. The corrected energy for the O_2 molecule is used[43].

C. Post–Processing Modifications of DFT Results

For improved accuracy, we address the deficiencies of DFT and the use of finite sized supercells via a systematic application of post–processing modifications to the computed quantities in Eq. (1). These modifications include: (i) a scissors–shift of conduction band states, including shifting defect levels for all shallow donors, to the experimental band gap for STO, (ii) a shift of the deep Kohn–Sham levels found in V_{OO} and V_{SrOOb} according to GGA+U calculations, (iii) the elimination of Moss–Burnstein band–filling effects arising from the use of finite–sized supercells, (iv) the alignment of background potential for charged supercells, and (v) an estimate of the screened interaction energy of charged supercells.

Scissors operator for band gap corrections. Band gap corrections are estimated by applying a scissors operator to the conduction bands to open the gap from the DFT–PBE value of $E_g^{PBE} = 1.82$ eV to the experimental value of $E_g^{exp} = 3.25$ eV; total energies ($E_{D,q}$ in Eq. 1) of supercells containing occupied shallow donor states are accordingly adjusted. This applies to the oxygen vacancy V_O and the vacancy complexes V_{OO}, $V_{SrOO,a}$, and $V_{SrOO,b}$.

Shifting deep defect levels with respect to band edges. In agreement with Ref. [28], we find that the application of a Hubbard U of 5.0 eV to improve the description of the on–site Coulomb interaction of the Ti 3d orbitals results in the opening of the gap to $E_g^{PBE+U} = 2.45$ eV. We also find that, relative to their position in PBE, within PBE+U the deep Kohn–Sham defect levels for V_{OO} and $V_{SrOO,b}$ are shifted down from the conduction band edge by an additional ΔE_{sh} = -0.71 eV and -0.62 eV respectively. Therefore, we adjust these defect supercell energies $E_{D,q}$ by

$$\Delta E_{KS} = m\Delta E_{sh}\left(\frac{E_g^{exp} - E_g^{PBE}}{E_g^{PBE+U} - E_g^{PBE}}\right) , \tag{3}$$

where m denotes the occupancy of the deep Kohn–Sham defect level.

Moss–Burnstein band–filling correction. Supercell calculations model systems at very high defect concentrations, whereas physically one is usually interested in the dilute defect limit. The high defect concentrations simulated exhibit Moss–Burnstein band–filling effects[44,45], in which spurious defect–defect interactions result in band distortion. The unphysical band–filling effects are eliminated in the manner described in Ref. [46] for all shallow vacancies and vacancy complexes considered. We note that for the $4 \times 4 \times 4$ supercell considered here, the band–filling effects are quite small (generally < 0.1 eV).

Alignment of valence band maxima for charged supercells. Total energies of supercells computed by DFT calculations within the pseudopotential momentum–space formalism[47] are given with respect to the average total electrostatic potential within the supercell. Particularly for the case of charged supercell calculations, it is necessary to ensure that the average electrostatic potentials are aligned for the pure (neutral) host and the charged defect system so that total energies can be consistently compared. Thus, a potential alignment term is added to the defect formation energy in Eq. 1, as described in Ref. [46]:

$$\Delta E_{PA}(D, q) = q(V_{D,q}^r - V_H^r) \tag{4}$$

where the reference potentials V^r within the host H and the charged defect (D, q) supercells are determined by averaging the electrostatic potentials in spheres around atomic sites located far from the defect.

Finite size extrapolation for charged defect–defect interactions. Finally, for charged supercells, the screened interaction energy of the periodically arranged charged defect and the compensating background is estimated by the extrapolation approach described in Refs. [48], [49], and [50]. This approach estimates the charged defect–defect interaction energy arising from the use of supercells with periodic boundary conditions to $\mathcal{O}(L^{-5})$. Figure 2 illustrates the extrapolation for the singly charged oxygen vacancy V_O^{+1} for supercells of size $n \times n \times n$, $n = 2, 3, 4, 5$. The curved line shows the fit

$$E_T(\frac{1}{L}) = E_T(\frac{1}{L} \rightarrow 0) - \frac{A}{L} - \frac{B}{L^3} \ , \tag{5}$$

in which L^3 denotes the volume of the supercell and A, B are the parameters. To construct this curve, we have use unrelaxed defect geometries and have eliminated the Moss–Burnstein band–filling effects described in the paragraph above. We have found, as suggested by Ref. [51], that the Makov–Payne[52] approximation greatly overestimates the charged defect interaction energy, and that finite size extrapolation is a better approach to estimating this correction. For this system, enhanced screening (thanks to the large dielectric constant of STO) results in relatively small charged defect interactions, and convergence to energies within 0.2 eV is achieved for supercells of size $4 \times 4 \times 4$ and larger.

Before concluding this section, we note that the uncertainties created by band gap problems, the use of finite–sized supercells, and the approximations introduced by the post–processing modifications make it nearly impossible to determine quantitatively accurate defect formation energies. To the extent possible, we have invoked estimates of corrections to band gap and finite size effect errors in a systematic and consistent manner; overall, we find that for most reasonable choices of post–processing corrections, qualitatively our results remain unchanged and our conclusions and results remain unaltered.

D. Point–Defect Formation Energies

Defect–formation energies computed at three points corresponding to low, middle, and high $\Delta\mu_O$ on path λ^1 (of Fig. 1) are shown in Fig. 3. These are plotted as a function of the Fermi energy E_F, which would be in the middle of the gap for intrinsic, stoichiometric STO, and is higher (lower) for n (p) –type STO. In Fig. 3, we assume that E_F is an independent (externally–controlled) parameter whose value can be fixed via, *e.g.*, the incorporation of impurity dopants such as Lanthanum. For $\Delta\mu_O = \Delta\mu_O^{min}$ (first panel), the most favorable defects are, not unexpectedly, V_O and V_{OO} in various charge states. Ionized V_{Sr} and V_{Ti} only become competitive at high E_F, serving as compensating acceptors. By contrast, for the highest $\Delta\mu_O = 0$ (Fig. 3, third panel), the most favorable defects are V_{Sr} and V_{Ti}. V_O only become favorable at low E_F, serving here as compensating donors. For mid–ranged $\Delta\mu_O = \lambda^1_{min}/2$ (Fig. 3, middle panel), as E_F increases, the lowest energy defect shifts from V_O^{+2}, the oxygen vacancy in the plus 2 two ionized state, to V_{Sr}^{-2}. At the mid–ranged values of E_F, both V_O^{+2} and V_{Sr}^{-2} are present and may bind together to form the electronically neutral Schottky defect V_{SrO}. Overall, we note two trends from Fig. 3. First, as $\Delta\mu_O$ increases, the minimum energy defects shift from (V_O, V_{OO}) to (V_{Sr}, V_{Ti}), as oxygen vacancies are less favorable (and cation vacancies more favorable) in oxygen rich environments. Second, as E_F increases from the valence to conduction band edge, the minimum energy defect shifts from (V_O, V_{OO}) to (V_{Sr}, V_{Ti}) due to the favorability of forming compensating defects. According to this analysis, compensation mechanisms provide an inherent limitation to the dopability of $SrTiO_3$ (similar to, *e.g.*, the amphoteric defect model[53]).

E. Point–Defect Phase Diagrams

Using the formalism developed here, we now assess the effect of Sr–poor and Ti–poor growth conditions on the defect distributions. PLD is one of the versatile thin film growth processes with a complex interplay of parameters determining the growth of the thin film material. Laser fluence is a common non–equilibrium growth parameter which can be used to tailor the film growth. For example, recent experiments indicate that nonstoichiometric transfer from ceramic targets to films in the PLD process, induced by preferential ablation from the target, can affect Sr/Ti stoichiometry[16,17]. Further, positron lifetime measurements indicate that the Sr/Ti stoichiometry can be controlled by laser fluence[17]. Meanwhile, our interest is to explore the role of parameters such as oxygen partial pressure and chemical potential (doping level). In Fig. 4, we present point–defect phase diagrams, in which the dominant (lowest formation energy) defect is indicated as a function of $\Delta\mu_O$ and E_F for the three paths λ^1, λ^2, and λ^3 in Fig. 1. In this figure, the La–dopant concentrations are calculated self–consistently using the charge–neutrality constraint and the mass–action law. In the left panel of Fig. 4 (path λ^1, nominally normal Sr/Ti stoichiometry), the dominant defects are shown to be V_O^{+2}, V_{Sr}^{-2}, and V_{Ti}^{-4}. The two trends discussed above are evident in this panel: the defect distribution shifts from anion to cation vacancies with increasing $\Delta\mu_O$ and increasing E_F. Note how reduced the effect of doping

with 15% La is due to the low formation energy of compensating V_{Sr}. In the middle panel of Fig. 4, the dominant defect is shown for the case of Sr–poor growth, corresponding to path λ^2 of Fig. 1. The two trends persist; however, the regime for which V_{Sr} and V_{SrO} are dominant is expanded. This growth regime would be particularly unfavorable for La–doping, as compensating V_{Sr} renders it very difficult to introduce free electrons. For the Ti–poor growth regime of path λ^3 (right panel, Fig. 4), the V_{Ti} regime grows at the expense of V_{Sr} and V_{SrO}, and the capacity for external doping to create free electrons is recovered due to the overall higher formation energy of the prevailing compensating species V_{Ti}. If indeed the Sr/Ti ratio can be controlled by laser fluence[17], the three panels of Fig. 4 suggest a reason for the seemingly contradictory reports of vacancy defect characteristics that have been reported for PLD growth in terms of a high sensitivity of the defect distribution to the growth conditions. Our analysis suggests that target growth windows, in terms of Sr/Ti stoichiometry, can maximize the effects of extrinsic doping, illustrating how controlled use of laser fluence, oxygen pressure, and dopant concentration may offer routes to more controlled defect compositions and film properties in PLD–grown systems.

III. EXPERIMENTS AND DISCUSSION

The phase diagrams presented in Fig. 4 indicates that careful control over thermodynamic parameters may result in tunability of defect profiles. To explore the applicability of the point defect analysis to real STO thin films, we synthesize and characterize a number of STO thin films via PLD as described below. Strictly (as discussed above), the applicability of the thermodynamic framework is best–suited for thin films grown under near–equilibrium conditions and a quantitative comparison is not expected. However, we wish to assess whether thermodynamic variables such as oxygen partial pressure and electron chemical potential affect the stoichiometry of films grown via high–energy techniques such as PLD, and whether this effect can be qualitatively explained using the thermodynamic framework developed above.

Thin films of doped STO were grown using pulsed laser deposition. These films were grown using a KrF excimer laser with a laser fluence of 1.5 J cm^{-2} over a range of growth pressures (in oxygen partial pressure P_{O_2}) from 100 mTorr to 10^{-8} Torr. To minimize the possibility that non-stoichiometry could arise from different ablation conditions, we grew all the samples with the same fluence and spot area, and we have used the same laser fluence as in Ref. [21], which we believe to be optimal for stoichiometric transfer. The growth temperature as measured by the thermocouple attached to the substrate heater was set as 850°C. The oxygen partial pressure during the growth was varied between 10^{-1} and 10^{-8} Torr, and targets with La doping of 0,2,5,10 and 15% in STO were used to control the amount of La doping. X–ray diffraction measurements for our samples demonstrate the high crystallinity of the films used in our investigation. We do not observe Ruddlesden–Popper type defects in our systems, which we believe is because our choice of growth parameters do not correspond to Sr–rich growth regimes.

Carrier concentrations in the as–grown films are obtained via Hall effect measurements. Figure 5 shows the measured electron carrier concentration as a function of the La content of the ceramic targets for growth under different oxygen pressures P_{O_2}. In Fig. 5, the measured carrier concentrations show a large dependence on P_{O_2}, demonstrating that thermodynamic parameters influence the properties of PLD–grown thin films. The measured carrier concentrations are generally lower than expected from the La doping alone if the thin films were otherwise stoichiometric (indicated by the dotted line). This observation is consistent with the presence of compensating species such as V_{Sr} and V_{Ti} predicted by the point–defect analysis. Further, the measured carrier concentrations parallel the trends we identified in Figs. 3 and 4. For instance, we note that for a fixed La concentration, the measured carrier concentration in Fig. 5 (and thus E_F) decreases as P_{O_2} increases. This trend can also been seen in the phase diagrams of Fig. 4, in which the lower defect formation energies of the compensating cation vacancies at high P_{O_2} serve to reduce the measured carrier concentrations at fixed La–doping. By contrast, at low P_{O_2} the measured carrier concentrations are higher, because the defect profile shifts towards oxygen vacancies and renders the formation of the compensating cation vacancies more difficult.

We note that experimentally accessible values of T and P_{O_2} correspond to -2 eV $< \Delta\mu_O <$ 0 eV according to data in Ref. [41]; this corresponds roughly to the second and third panel of Fig. 3. In this regime, when STO is doped with donors such as La, cation vacancies exhibit the lowest formation energies. It is interesting that in most PLD–grown STO, the existence of V_O has been long documented whereas the cation vacancies V_{Sr} and V_{Ti} have traditionally received less attention. However, their relevance has also recently become more appreciated: they have been implicated in defect–induced ferroelectricity[13,14] as well as the suppression of donor doping in STO[16]. Signatures of their existence have recently been observed in PLD grown homoepitaxial STO layers via positron annihilation lifetime spectroscopy measurements[17], and the lattice constant expansion that is often observed in PLD–grown films and attributed to V_O was shown to also be consistent with cation vacancies[16]. Our analysis suggests that the presence of V_O arises mainly from the kinetic inhibition of oxygen incorporation into the growing thin film (as they are not favored by their equilibrium formation energies), resulting in locally much lower $\Delta\mu_O$ than the experimentally accessible range.

Hence, the point–defect analysis is consistent with the presence of both cation and anion vacancies, and suggests that their relative concentrations can be tuned by P_{O_2} and/or degree of external doping as suggested in Figs. 3 and 5. We also comment on V_{OO}, because oxygen vacancy clustering is often implicated in the blue light emission observed in STO[28]: according to our analysis and in contrast to the findings of Ref. [28], when charged defects are considered, we find that clustering of V_O is not particularly favorable, a result of the electrostatic repulsion arising from the fact that V_O tend to be charged.

To further explore whether the sensitivity of the carrier concentration to P_{O_2} during growth observed in Fig. 5 can be attributed to stoichiometric variations, we perform time of flight – ion scattering and recoil spectroscopy (TOF–ISARS) measurements[54,55] on our samples. In these measurements (see inset in Fig. 6a), a primary ion beam of ^{39}K ions with a kinetic energy of 10 keV is directed at the sample. An Ionwerks (Houston, USA) Mass Spectrometry of Recoiled Ions (MSRI) Reflectron detector was used to detect the recoiled species. The MSRI detector was fixed at a 60° angle to the incident ion beam. The angles of incidence used at the sample are 15° and 30° (for the 30° case, the shadowing regions and blocking cones are directed more downward, which is expected to give a better representation of the subsurface film layers). Figure 6 plots the relative intensities for various atomic species registered by the MSRI detector, normalized to the primary ion signal, and plotted as a function of the azimuthal angle δ (denoting the orientation of the film surface with respect to the incident beam). The minima and maxima in the spectra reflect the crystalline directions where different species are blocking each other or presenting a free path, respectively.

Data is shown for both pure and La–doped STO grown under high and low P_{O_2}. Fig. 6a shows the TOF relative intensity for Sr and La recoiled from La-doped STO films grown at both low and high P_{O_2}. While the La signal is similar for the two growth pressures, a clear difference is observed in the Sr signal. Consistent with our Hall measurements, the Sr intensity is higher at low P_{O_2}, suggesting that growth at low P_{O_2} results in the incorporation of more Sr into the films. This is also consistent with our point–defect analysis, which suggests a shift from V_{Sr} to V_O as the oxygen partial pressure decreases to further inhibit the formation of carrier–compensating defects. Thus, even under high–energy (non–equilibrium) growth conditions, it appears that thermodynamic quantities such as growth pressure and defect formation energies exhibit an influence on the defect characteristics of the films. In Fig. 6b and 6c, TOF results are shown for pure STO for incident angles of 15° and 30°, respectively. Again, the difference in the Sr signals for growth at high and low P_{O_2} is clearly observable (particularly near the peaks in Fig. 6c). These results indicate that, even in undoped STO, systems grown at low P_{O_2} are more Sr rich than those grown at high P_{O_2}; this is consistent with the point–defect model and the carrier concentration measurements, which predict a shift from anion to cation vacancies as P_{O_2} increases. Although the result of variable cation stoichiometry with P_{O_2} may be surprising, similar observations have been previously reported. For example, our observation is in excellent agreement with investigations on the electrical conductivity as a function of oxygen pressure on thin films and crystals of STO[56] and with the demonstration of the use of P_{O_2} for controlled cation stoichiometry in STO thin films[57].

Finally, we give an example of the application of our analysis to the recent demonstration of transparent conducting oxides (TCO) made from double–doped STO[20]. The unusual combination of electronic and optical properties that are necessary for a material to conduct electrons while remaining transparent to visible light is most often related to the presence of shallow donor states close to the conduction band. For instance, in Indium Tin Oxide (ITO), both doping with tin and V_O provide shallow donor states from which electrons are thermalized at room temperature into the conduction bands. Our analysis suggests that V_O are responsible for the shallow donor states that give rise to conduction in STO (as with ITO). Based on Figs. 3 and 4, transition levels for V_O appear close to the conduction band edge (green circles in Fig. 3). Further, in undoped STO, the number of oxygen vacancies are roughly offset by the number of strontium vacancies (for instance, in Fig. 4, left panel), and the oxygen defect levels are thus mostly empty. However, incorporation of the appropriate quantities of La dopants through non–equilibrium doping, especially in growth regimes when compensation mechanisms are unfavorable, may provide avenues to control the filling of these defect levels as necessary to achieve a TCO, as indicated in Ref. [20].

EE and JCG acknowledge the support of DOE grant DE-SC0002623. Calculations were performed in part at the National Energy Research Scientific Computing Center of the Lawrence Berkeley National Laboratory and in part by the National Science Foundation through TeraGrid resources provided by NCSA under grant TG-DMR090027. The research at Berkeley was supported by the Division of Materials Sciences and Engineering, Office of Basic Energy Sciences, U.S. Department of Energy, under contract No. DE–AC02–05CH11231. J.R. acknowledges the support of the Link Foundation.

* e-mail:elif1@mit.edu
† e-mail:jcg@mit.edu

[1] H. Takagi and H. Y. Hwang, Science **327**, 1601 (2010).
[2] J. Mannhart and D. G. Schlom, Science **327**, 1607 (2010).
[3] S.-W. Cheong and M. Mostovoy, Nat. Mater. **6**, 13 (2007).
[4] Y.-H. Chu, L. W. Martin, M. B. Holcomb, M. Gajek, S.-J. Han, Q. He, N. Balke, C.-H. Yang, D. Lee, W. Hu, Q. Zhan, P.-L. Yang, A. Fraile-Rodriguez, A. Scholl, S. X. Wang, and R. Ramesh, Nat. Mater. **7**, 478 (2008).
[5] J. Y. Jo, R. J. Sichel, H. N. Lee, S. M. Nakhmanson, E. M. Dufresne, and P. G. Evans, Phys. Rev. Lett. **104**, 207601 (2010).
[6] S. J. May, P. J. Ryan, J. L. Robertson, J.-W. Kim, T. S. Santos, E. Karapetrova, J. L. Zarestky, X. Zhai, S. G. E. te Velthuis, J. N. Eckstein, S. D. Bader, and A. Bhattacharya, Nat. Mater. **8**, 892 (2009).
[7] Y. Tokura, Rep. Prog. Phys. **69**, 797 (2006).
[8] V. Garcia, S. FUsil, K. Bouzehouane, S. Enouz-Vedrenne, N. D. Mathur, A. Bathelemy, and M. Bibes, Nature **460**, 81 (2009).
[9] Y. Kozuka, M. Kim, C. Bell, B. G. Kim, Y. Hikita, and H. Y. Hwang, Nature **462**, 487 (2009).
[10] K. Szot, W. Speier, G. Bihlmayer, and R. Waser, Nat. Mater. **5**, 312 (2006).
[11] C. Cen, S. Thiel, G. Hammerl, C. W. Schneider, K. E. Andersen, C. S. Hellberg, J. Mannhart, and J. Levy, Nat Mater **7**, 398 (2008).
[12] S. V. Kalinin, B. J. Rodriguez, A. Y. Borisevich, A. P. Baddorf, N. Balke, H. J. Chang, L.-Q. Chen, S. Choudhury, S. Jesse, P. Maksymovych, M. P. Nikiforov, and S. J. Pennycook, Adv. Mater. **22**, 314 (2010).
[13] M. Choi, F. Oba, and I. Tanaka, Phys. Rev. Lett. **103**, 185502 (2009).
[14] H. W. Jang, A. Kumar, S. Denev, M. D. Biegalski, P. Maksymovych, C. W. Bark, C. T. Nelson, C. M. Folkman, S. H. Baek, N. Balke, C. M. Brooks, D. A. Tenne, D. G. Schlom, L. Q. Chen, X. Q. Pan, S. V. Kalinin, V. Gopalan, and C. B. Eom, Phys. Rev. Lett. **104**, 197601 (2010).
[15] J. Son, P. Moetakef, B. Jalan, O. Bierwagen, N. J. Wright, R. Engel-Herbert, and S. Stemmer, Nature Mater. **9**, 482 (2010).
[16] T. Ohnishi, K. Shibuya, T. Yamamoto, and M. Lippmaa, J. Appl. Phys. **103**, 103703 (2008).
[17] D. J. Keeble, S. Wicklein, R. Dittmann, L. Ravelli, R. A. Mackie, and W. Egger, Phys. Rev. Lett. **105**, 226102 (2010).
[18] T. Ohnishi, M. Lippmaa, T. Yamamoto, S. Meguro, and H. Koinuma, Appl. Phys. Lett. **87**, 241919 (2005).
[19] D. Kan, T. Terashima, R. Kanda, A. Masuno, K. Tanaka, S. Chu, H. Kan, A. Ishizumi, Y. Kanemitsu, Y. Shimakawa, and M. Takano, Nat. Mat. **4**, 816 (2005).
[20] J. Ravichandran, W. Siemons, H. Heijmerikx, M. Huijben, A. Majumdar, and R. Ramesh, Chem. Mater. **22**, 3983 (2010).
[21] D.-W. Oh, J. Ravichandran, C.-W. Liang, W. Siemons, B. Jalan, C. M. Brooks, M. Huijben, D. G. Schlom, S. Stemmer, L. W. Martin, A. Majumdar, R. Ramesh, and D. G. Cahill, Appl. Phys. Lett. **98**, 221904 (2011).
[22] B. Jalan, P. Moetakef, and S. Stemmer, Appl. Phys. Lett. **95**, 032906 (2009).
[23] C. M. Brooks, L. F. Kourkoutis, T. Heeg, J. Schubert, D. A. Muller, and D. G. Schlom, Appl. Phys. Lett. **94**, 162905 (2009).
[24] D. J. Keeble, B. Jalan, L. Ravelli, W. Egger, G. Kanda, and S. Stemmer, Appl. Phys. Lett. **99**, 232905 (2011).
[25] N. Shanthi and D. D. Sarma, Phys. Rev. B **57**, 2153 (1998).
[26] W. Luo, W. Duan, S. G. Louie, and M. L. Cohen, Phys. Rev. B **70**, 214109 (2004).
[27] A. M. Kolpak and S. Ismail-Beigi, Phys. Rev. B **83**, 165318 (2011).
[28] D. D. Cuong, B. Lee, K. M. Choi, H.-S. Ahn, S. Han, and J. Lee, Phys. Rev. Lett. **98**, 115503 (2007).
[29] M. Jourdan and A. Hermann, Physica C **388**, 509 (2010).
[30] W. Siemons, G. Koster, H. Yamamoto, W. A. Harrison, G. Lucovsky, T. H. Geballe, D. H. A. Blank, and M. R. Beasley, Phys. Rev. Lett. **98**, 196802 (2007).
[31] K. Koumoto, Y. Wang, R. Zhang, A. Kosuga, and R. Funahashi, Annu. Rev. Mater. Res. **40**, 363 (2010).
[32] J. H. Haeni, P. Irvin, W. Chang, R. Uecker, P. Reiche, Y. L. Li, S. Choudhury, W. Tian, M. E. Hawley, B. Craigo, A. K. Tagantsev, X. Q. Pan, S. K. Streiffer, L. Q. Chen, S. W. Kirchoefer, J. Levy, and D. G. Schlom, Nature **430**, 758 (2004).
[33] K. Ueno, S. Nakamura, H. Shimotani, A. Ohtomo, N. Kimura, T. Nojima, H. Aoki, Y. Iwasa, and M. Kawasaki, Nature Mater. **7**, 855 (2008).
[34] A. Ohtomo and H. Y. Hwang, Nature **427**, 423 (2004).
[35] Y. S. Kim, J. Kim, S. J. Moon, W. S. Choi, Y. J. Chang, J.-G. Yoon, J. Yu, J.-S. Chung, and T. W. Noh, Appl. Phys. Lett. **98**, 202906 (2009).
[36] T. Mizoguchi, H. Ohta, H.-S. Lee, N. Takahashi, and Y. Ikuhara, Adv. Func. Mater. **21**, 2258 (2011).
[37] http://www.q-espresso.org.
[38] D. Vanderbilt, Phys. Rev. B Rapid Commun. **41**, 7892 (1990).
[39] J. P. Perdew, K. Burke, and M. Ernzerhof, Phys. Rev. Lett. **77**, 3865 (1996).
[40] Rigorously, for a defect–forming reaction at a given temperature and pressure, the governing thermodynamic potential is the Gibbs free energy $\Delta G_{D,q}(T, P_i)$; however, we assume that the entropic contribution to and the pressure dependence of the free energy are negligible compared to the internal energy contribution, so that $\Delta G_{D,q}(T, P_i) \approx \Delta E_{D,q}$.
[41] "Nist chemistry webbook," (2011), online: http://webbook.nist.gov.
[42] E. Takayama-Muromachi and A. Navrotski, J. Solid State Chem. **72**, 244 (1988).
[43] Y. Zhang and W. Yang, Phys. Rev. Lett. **80**, 890 (1998).

[44] T. S. Moss, Proc. Phys. Soc. London, Sect. B **67**, 775 (1954).
[45] E. Burnstein, Phys. Rev. **93**, 632 (1954).
[46] S. Lany and A. Zunger, Phys. Rev. B **78**, 235104 (2008).
[47] J. Ihm, A. Zunger, and M. L. Cohen, J. Phys. C **12**, 4409 (1979).
[48] C. W. M. Castleton, A. Hoglund, and S. Mirbt, Phys. Rev. B **73**, 035215 (2006).
[49] J. Shim, E.-K. Lee, Y. J. Lee, and R. M. Nieminen, Phys. Rev. B **71**, 035206 (2005).
[50] N. D. M. Hine, K. Frensch, W. M. C. Foulkes, and M. W. Finnis, Phys. Rev. B **79**, 024112 (2009).
[51] T. Tanaka, Katsuyuki, Y. Ikuhara, and T. Yamamoto, Phys. Rev. B **68**, 205213 (2003).
[52] G. Makov and M. C. Payne, Phys. Rev. B **51**, 4014 (1995).
[53] W. Walukiewicz, Physica B **302–303**, 123 (2001).
[54] W. J. Rabalais, *Principles and Applications of Ion Scattering Spectrometry: Surface and Chemical and Structural Analysis* (Wiley Interscience, 2002).
[55] A. Biswas, P. Rossen, C.-H. Yang, W. Siemons, M. Jung, I. Yang, R. Ramesh, and Y. Jeong, Appl. Phys. Lett. **98**, 051904 (2011).
[56] C. Ohly, S. Hoffmann-Eifert, X. Guo, J. Schubert, and R. Waser, J. Am. Ceram. Soc. **89**, 2845 (2006).
[57] Y. Kozuka, Y. Hikita, C. Bell, and H. Y. Hwang, Appl. Phys. Lett. **97**, 012107 (2010).

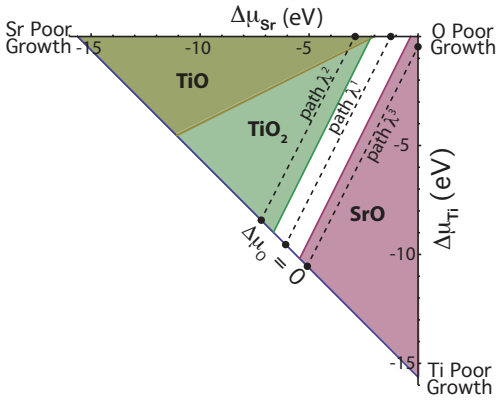

FIG. 1. (Color online). Chemical potential phase space: each point in the triangle satisfies $\Delta\mu_{Sr} + \Delta\mu_{Ti} + 3\Delta\mu_O = \Delta\mu_{STO}$. In the white region, STO is stable; in the shaded regions formation of different phases (indicated) is favorable.

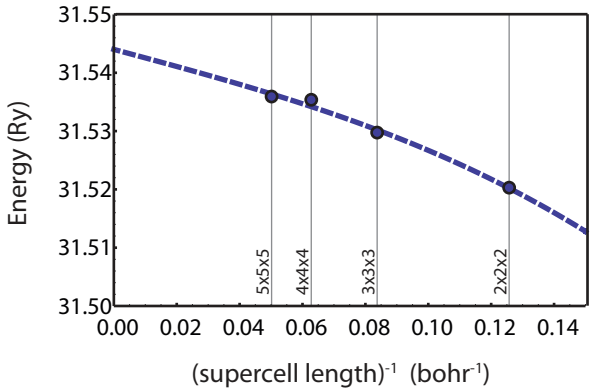

FIG. 2. (Color online). Finite size extrapolation to estimate the energy of charged defect–defect interactions for the singly charged oxygen vacancy V_O^{+1}. The line is the fit to the data based on Eq. 3.

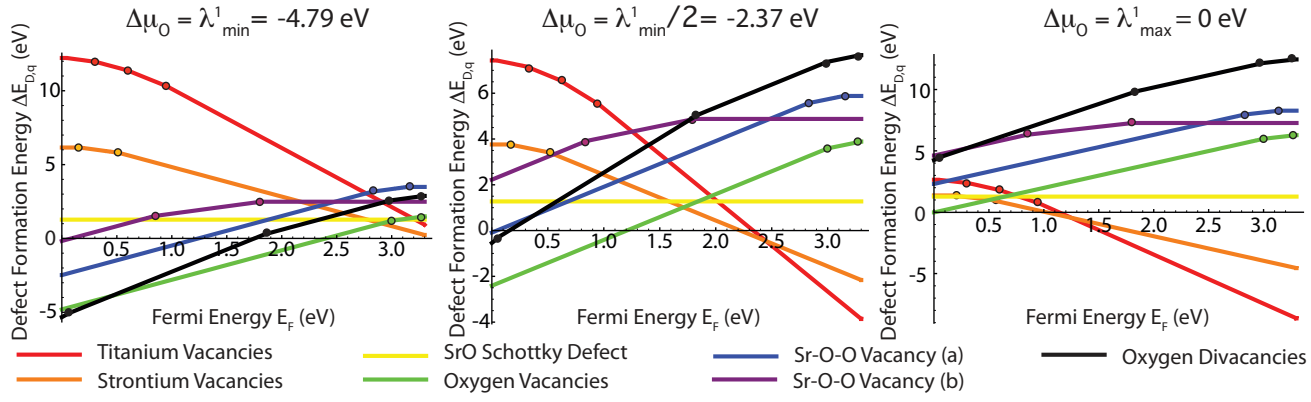

FIG. 3. (Color online). Defect formation energy as a function of the Fermi energy E_F for vacancies and vacancy complexes in STO. Defect formation energies are shown at three points along the path λ^1 in Fig. 1. $\Delta\mu_o = \lambda^1_{min}, \lambda^1_{min}/2, 0$ corresponds to low, mid–ranged, and high oxygen pressures, respectively. The circles correspond to defect transition levels. Two trends are evident. As the oxygen pressure increases, the most favorable defect changes from oxygen vacancies/vacancy complexes to strontium/titanium vacancies. As the Fermi level increases, the most favorable defect changes from oxygen vacancies/vacancy complexes (compensating donors) to strontium/titanium vacancies (compensating acceptors).

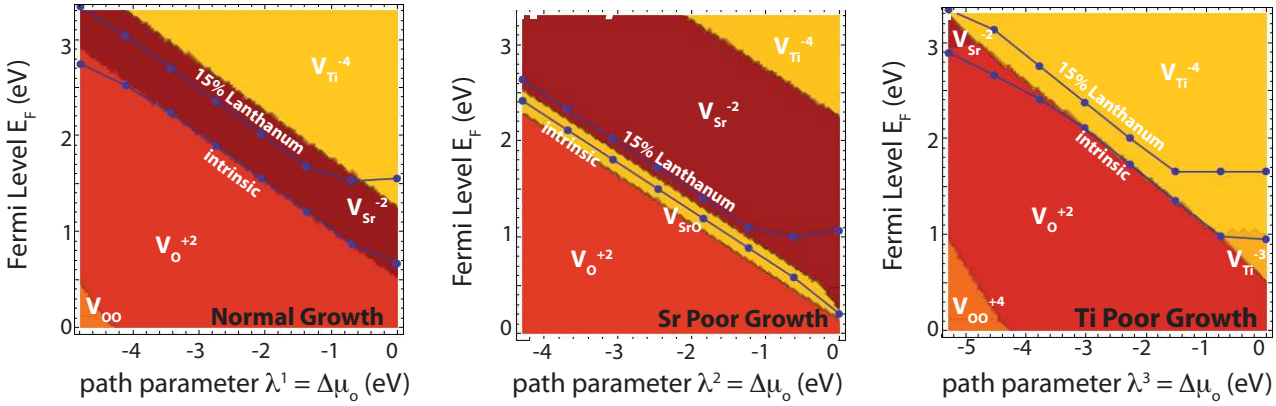

FIG. 4. (Color online). Plots showing the most favorable vacancy/vacancy complex for normal, Sr poor, and Ti poor prevailing thermodynamic conditions, as a function of chemical potential $\lambda = \Delta\mu_O$ and Fermi energy E_F. The La concentration is estimated from the charge neutrality constraint and the mass action law.

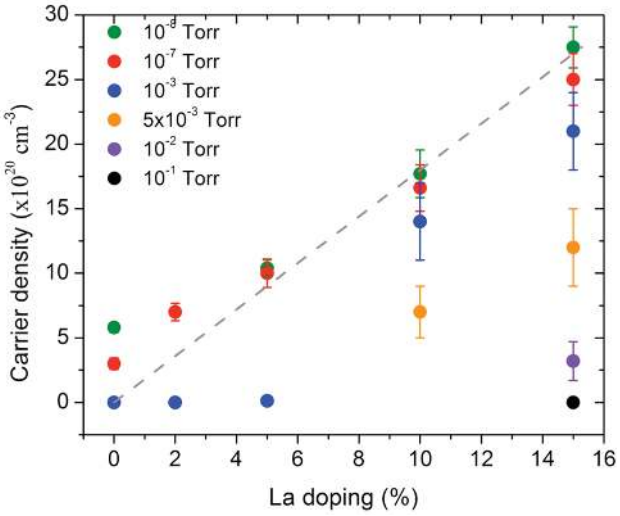

FIG. 5. (Color online). Carrier density, obtained from Hall effect measurements, of PLD–grown STO films vs. La content for growth at different oxygen partial pressures. Dashed line: carrier density predicted by La concentration in otherwise stoichiometric films. Measured carrier concentrations exhibit a large sensitivity to the oxygen partial pressure.

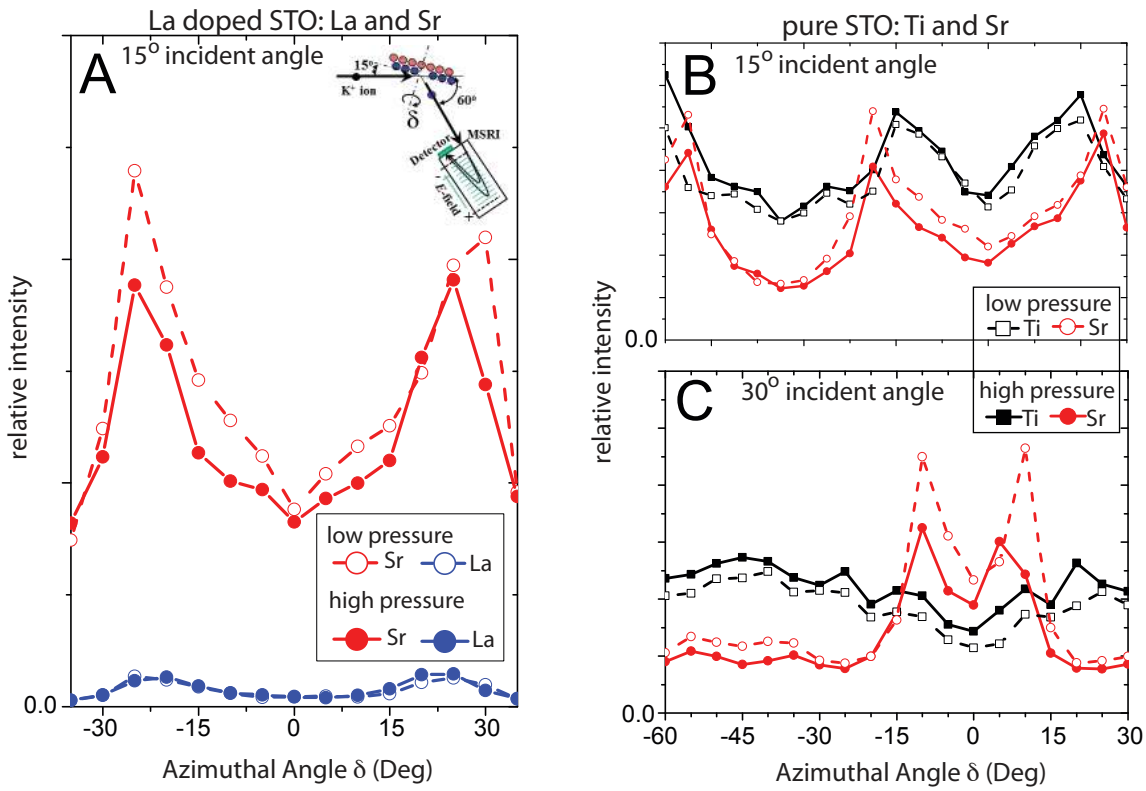

FIG. 6. (Color online). Time of Flight Ion Scattering and Recoil Spectroscopy measurements on pure and La–doped STO thin films indicate Sr–deficiency (or O–excess) when films are synthesized at high P_{O_2}. (a) Main: Counts registered by the MSRI detector, normalized to the scattered potassium signal, for La–doped STO grown at high and low P_{O_2}. Although the La signal is similar for both cases, the Sr signal is notably lower for films synthesized at high P_{O_2}. (The experimental setup is shown in the inset.) (b) and (c): Counts registered by the MSRI detector, normalized to the scattered potassium signal, for pure STO grown at high and low P_{O_2} for beam incident at 15° and 30° incident angles, respectively. Again, while Ti count is similar for high and low P_{O_2}, Sr count is smaller at high P_{O_2} and larger at low P_{O_2}.